Icarus 211 (2011) 913–916

Contents lists available at ScienceDirect

Icarus

journal homepage: www.elsevier.com/locate/icarus

Note

Scaling of melt production in hypervelocity impacts from high-resolution numerical simulations

Amy C. Barr [a,c,*], Robert I. Citron [b,c]

[a] Department of Space Studies, Southwest Research Institute, 1050 Walnut St., Suite 300, Boulder, CO 80302, United States
[b] Laboratory for Atmospheric and Space Physics, Campus Box 392, University of Colorado, Boulder, CO 80309, United States
[c] Center for Lunar Origin and Evolution, Southwest Research Institute, Boulder, CO 78228-0510, United States

ARTICLE INFO

Article history:
Received 6 May 2010
Revised 7 October 2010
Accepted 27 October 2010
Available online 4 November 2010

Keywords:
Impact processes
Cratering
Interiors

ABSTRACT

The volume of melt produced in hypervelocity planetary impacts and the size and shape of the melted region are key to understanding the impact histories of solid planetary bodies and the geological effects of impacts on their surfaces and interiors. Prior work of Pierazzo et al. (Pierazzo, E., Vickery, A.M., Melosh, H.J. [1997]. Icarus 127, 408–423) gave the first estimates of impact melt production in geological materials using a modern hydrocode and equation of state. However, computational limits at the time forced use of low resolution, which may have resulted in low melt volumes. Our simulations with 50 times higher resolution provide independent confirmation of the Pierazzo et al. (Pierazzo, E., Vickery, A.M., Melosh, H.J. [1997]. Icarus 127, 408–423) melt volumes in aluminum, iron, dunite, and granite impacts at velocities between 20 and 80 km/s. In ice/ice impacts, we find that melt volumes depend on target temperature and are lower than predicted by Pierazzo et al. (Pierazzo, E., Vickery, A.M., Melosh, H.J. [1997]. Icarus 127, 408–423). Our melt volumes are directly proportional to impact energy for all materials, over a wide range of impact velocity. We also report new data for melt volume scalings for ice/dunite and iron/dunite impacts and the size and shape of melted region, valuable for interpretation of cratering records and studies of impact-induced differentiation.

1. Introduction

Melting, vaporization, and shock heating during hypervelocity impacts affect many aspects of the surface (e.g., Grieve and Cintala, 1992; Cintala and Grieve, 1998; Abramov and Kring, 2005; Abramov and Mojzsis, 2009) and interior (Tonks and Melosh, 1992, 1993; Reese and Solomatov, 2006; Barr and Canup, 2010) evolution of terrestrial and icy worlds. The size and shape of melted region relative to crater size can be used to estimate impactor sizes, vital to interpretation of the cratering records of terrestrial planets (e.g., Cintala and Grieve, 1998). Hypervelocity impacts can also affect the interior structure of a planet by driving impact-induced differentiation, during which hypervelocity impacts onto a planet composed of a mixture of "heavy" and "light" material (e.g., rock + ice or iron + rock) melt the lighter phase, permitting the dense material to sink to the planet's center. This process is thought to occur in the late stages of terrestrial planet accretion (e.g., Tonks and Melosh, 1992) and in ice/rock satellites during the Late Heavy Bombardment (Tonks et al., 1997; Barr and Canup, 2010; Barr et al., 2010).

A hypervelocity impact onto the surface of a solid planet creates a shock wave that compresses the target beneath the impact site. After the shock wave passes, the planet's interior decompresses quasi-adiabatically, but net $P\Delta V$ work is done on a roughly hemispherical region beneath the impact point (see Melosh (1989) for discussion). A range of analytical and numerical techniques have been used to characterize the size, shape, and volume of region melted during an impact by focusing on the decay in peak shock pressure or material velocity as a function of distance beneath the impact point (e.g., Gault and Heitowit, 1963; O'Keefe and Ahrens, 1977; Croft, 1982; Kieffer and Simonds, 1980; Bjorkman and Holsapple, 1987; Grieve and Cintala, 1992; Tonks and Melosh, 1992). Numerical simulations of hypervelocity impacts in the pivotal study of Pierazzo et al. (1997) (hereafter, P97) show that the shape of the region shocked to the point of melting is close to that of a buried sphere, whose radius and depth of burial scale with the radius and velocity of the impactor. Melt volumes estimated from the P97 simulations agree with volumes in terrestrial impact craters, lending support to their particular methodology. Melt volumes for rocks and metals were shown to obey a pure energy scaling (cf., Bjorkman and Holsapple, 1987), but melt volumes for ice exhibited a different scaling with impact velocity consistent with porous materials (P97).

Although P97 used numerical techniques that were state-of-the-art for the time, computing limitations prevented a thorough exploration of parameter space at high resolution: a resolution of 20 grid cells-per-projectile radius (cppr) was used for the majority of simulations. A numerical resolution test for $5 < \text{cppr} < 40$ showed that 20 cppr was sufficient to determine melt volume to within 10%. However, because simulations with low numerical resolution tend to underestimate melt volumes (P97), it is advantageous to explore much higher resolutions given advances in computing speed.

Here, we provide independent verification of the results of P97 by determining scaling relationships for melt volumes and the size and shape of melted region using high-resolution simulations performed using the hydrocode CTH (McGlaun et al., 1990), a modern successor to the hydrocode used by P97. Impact-induced differentiation studies rely on knowledge of the size and shape of region shocked to >50% melting, within which the partially molten lighter material (silicate magma or ice/water slurry) has a rheology comparable to the liquid phase (Renner et al., 2000), permitting rapid separation of the heavy second material. The only comprehensive numerical study for the size and shape of this region was performed for ice by Barr and Canup (2010). Here, we extend those results to rocks, relevant to terrestrial planet evolution. We also determine melt volumes in (projectile/target) ice/dunite and iron/dunite impacts, relevant to an outer Solar System Late Heavy Bombardment (Levison et al., 2001; Gomes et al., 2005), and iron meteorite impacts onto terrestrial planets (Bottke et al., 2006).

2. Numerical methods

We perform numerical simulations of impacts using version of 9.1 of the CTH hydrocode (McGlaun et al., 1990). We simulate impacts between a 0.5 km-radius spherical projectile and a semi-infinite half-space in a 2-dimensional cylindrical

* Corresponding author at: Department of Space Studies, Southwest Research Institute, 1050 Walnut St., Suite 300, Boulder, CO 80302, United States. Fax: +1 303 546 9687.
E-mail address: amy@boulder.swri.edu (A.C. Barr).

0019-1035/$ - see front matter © 2010 Elsevier Inc. All rights reserved.
doi:10.1016/j.icarus.2010.10.022

domain 20 km wide and 15 km deep. The cylindrical domain requires a symmetry boundary condition on $x = 0$, and we impose transmitting boundary conditions on the other x and y boundaries. We use adaptive meshing subroutines in CTH to decrease element size in regions of high pressure and velocity, notably, along the shock front. Our numerical resolution varies as a function of location in the domain but achieves a maximum of 128 cppr. Fixed mesh simulations of 128 cppr produced similar results to adaptive mesh runs with a similar maximum resolution.

Melting occurs at locations in the target where the peak shock pressure (P_{sh}) exceeds the value required for complete melting. To determine how the peak shock pressure varies beneath the impact point, we embed tracer particles in the target initially located along lines spaced 10° apart between a vertical line beneath the impact point and the target surface (see Fig. 2 of P97 and Fig. S1 in Barr and Canup (2010)). Each line of tracers has 61 points spread in 160-m increments beneath the impact point to a distance 10 km (20 projectile radii) away. The tracers record pressures at time increments of 0.1 ms, and the pressure–time record from each tracer is analyzed to determine the peak shock pressure experienced during the impact. Our domain and tracer setup has been previously verified for aluminum/aluminum impacts using benchmarking data from Pierazzo et al. (2008). We are able to reproduce their peak shock pressure curves at the 2–5% level for 5 km/s and 20 km/s impacts.

We use the semi-analytical ANEOS equation of state package (Thompson and Lauson, 1972; Melosh, 2007), with library coefficients for aluminum and iron. We choose ANEOS over other equations of state (e.g., Tillotson) for consistency with prior work and because it easily allows us to determine where melting has occurred based on the material entropy. Important for our work, ANEOS provides physically realistic behavior close to the melting point for a wide range of materials, even though behavior in the vapor phase can deviate from experimental values for rock and ice (see Melosh (2007) for discussion). For consistency with P97, we use the Benz et al. (1989) dunite ANEOS, and the Westerly Granite ANEOS as a representative for granite (P97). We use ANEOS coefficients for water ice from Turtle and Pierazzo (2001), which have been used previously to study impact-induced melting on Europa. We do not include strength or fracture in our calculations because we are interested in peak shock pressures, which are achieved at early times during the contact and compression phase of the impact where these effects are unimportant (Melosh, 1989).

The pressure required for complete (P_{cm}) or incipient melting (P_{im}) is calculated using ANEOS outputs to determine where the Hugoniot in pressure–entropy space matches the entropy for complete (S_c) or incipient melting (S_i). The Hugoniot is calculated assuming that the target has a temperature equal to the reference temperature specified by ANEOS, which is 298 K for rock and metals. For water ice, the pressure for complete melting varies by a factor of ~2 as a function of temperature (cf., Stewart and Ahrens, 2005), ranging from 3.5 GPa at $T = 233$ K to 5.2 GPa at $T = 180$ K. We use an initial target temperature of 180 K for water ice, appropriate for outer planet satellite surfaces, and substantially lower than the ANEOS-specified melting temperature for water ice, 233 K. The target temperature used by P97 was ~230 K (E. Pierazzo, personal communication, 2010), which sets the initial entropy of the target comparable to the entropy for incipient melting, S_i. As we discuss below, our simulations with an initial target temperature of 230 K yield a completely melted region comparable in volume to P97. However, direct comparisons of the total melt volume are problematic because the entire domain has $S \sim S_i$.

Entropy and pressure values for complete and incipient melting are listed in Table 1. The pressure required to shock to 50% melt (P_{cr}) is calculated assuming that melt fraction is proportional to entropy (Tonks and Melosh, 1993),

$$\phi_m = \frac{S_{cr} - S_i}{S_c - S_i}, \tag{1}$$

where $\phi_m = 0.5$, and finding the pressure on the Hugoniot where S_{cr} is achieved.

3. Size and shape of melted region

The size and shape of the melted region are determined by finding the location on each tracer line where $P_{sh} = P_{cm}$ for complete melting, and likewise for P_{im} and P_{cr}. Tracer lines between $\theta = 0°$ (vertical) and $\theta = 80°$ from vertical are used to determine the boundary of the melted region ($\rho(\theta)$). We fit a circle to the $\rho(\theta)$ points to determine the radius (r) and depth of burial (z) of the region melted to $\phi = 1$ (complete melting), $\phi = 0.5$ (50% melting), and $\phi > 0$ (incipient melt). We report values normalized by impactor radius, $\chi = r/r_p$, $\xi = z/r_p$ (cf., Barr and Canup 2010). Fig. 1a illustrates how χ_{cm} and ξ_{cm} vary as a function of impact velocity. Trends are similar for the 50% and incipient melt regions. We use linear regression in log–log space to fit the χ data to a power law of form (cf., Barr and Canup 2010),

$$\chi = a_\chi \left(\frac{u}{40\ \mathrm{km/s}} \right)^{b_\chi}, \tag{2}$$

where impact velocity (u) is normalized using $u = 40$ km/s as a representative value. Similarly, the ξ data are fit to a function of form,

$$\xi = a_\xi \left(\frac{u}{40\ \mathrm{km/s}} \right)^{b_\xi}. \tag{3}$$

Fig. 1a illustrates a comparison between the χ and ξ data for complete melting and fits using Eqs. (2) and (3). Table 2 lists the values of a_χ, b_χ, a_ξ, and b_ξ for each material for the complete, 50%, and incipient melt regions. In general, we find χ and ξ values for the melted regions similar to those reported by P97. We note that our fits should not be used to extrapolate χ and ξ to impact velocities much lower than values shown in Fig. 1. As impact velocities decrease, values of b_χ and b_ξ increase, so that χ and ξ become very small as the peak shock pressure achieved in the impact approaches the peak pressure for melting (see Fig. 10 of P97).

4. Melt volumes

The vast majority of melt created in an impact is produced in the volume carved out by the buried sphere describing the completely melted region. This region has a volume $V = (4/3)\pi r^3 - (1/3)\pi(r-d)^2(2r+d)$. However, some partial melting occurs in the spherical shell in between the complete melting and incipient melting spheres. Following the methods of P97, we divide this shell into ten spherical sub-shells, within which the fraction of melt is calculated by converting the peak pressure to entropy using ANEOS, then using Eq. (1) to calculate ϕ. We compute the volumes contained by the inner and outer edges of each shell to give a total shell volume. Because the center of the incipient melting region is slightly below the center of the completely melted region, each shell is thicker at its base than at the top. The amount of melt contained in the zone of partial melting accounts for only a small percentage of the melt volume because $\chi_{cm} \sim \chi_{im}$. Fig. 1c shows how melt volumes vary as a function of cppr for impacts between an ice target/projectile at 10 km/s, an aluminum target/projectile at 20 km/s, and dunite/dunite impact at 20 km/s. For resolutions higher than 32 cppr, the change in melt volume due to increasing resolution is <5%. Our resolution testing agrees with tests performed by P97; 20 cppr underestimates melt volumes by only ~10%.

Melt volumes are normalized against projectile volume, $V_{proj} = (4/3)\pi r_p^3$, and we plot them as a function of melt number, u^2/E_M, where E_M is the melt energy (Bjorkman and Holsapple, 1987; P97). Table 1 lists melt energy values, calculated from ANEOS outputs by determining the specific energy along the Hugoniot where complete melting is achieved (E. Pierazzo, personal communication 2010). Bjorkman and Holsapple (1987) suggest that melt volume scales with melt number,

$$\log_{10}\left(\frac{V_m}{V_{proj}}\right) = a + \frac{3}{2}\mu \log_{10}\left(\frac{u^2}{E_M}\right). \tag{4}$$

For $u^2/E_M < 50$, Bjorkman and Holsapple (1987) suggest that $\mu = 2/3$, indicating that melt volumes scale linearly with impact energy, and volumes for larger melt numbers obey a momentum scaling ($\mu < 2/3$).

The solid symbols in Fig. 1d show how V_m/V_{proj} scale with melt number for like/like impacts for aluminum, iron, ice, dunite, and granite. For all materials, including ice, in the range $30 < u^2/E_M < 4500$, $a = -0.482$. We find that $\mu = 0.624$, close to the value for an energy scaling. For rocks and metals, P97 found $\mu = 0.708 \pm 0.039$, close to the value for an energy scaling, as well. We have included the iron/dunite and ice/dunite points for comparison in Fig. 1d, but do not expect them to have the same a value as for like/like impacts, and thus, did not include them in the fit. For ice/dunite, we find $a = -1.78$ and $\mu = 0.819$, and for iron/dunite, $\mu = 0.657$ and $a = -0.324$.

Overall, our results are consistent with P97, except in the case of ice/ice impacts. P97's melt volumes in ice were 10 times higher than for rocks and metals and fell along $\mu = 0.432$, similar to $\mu = 0.4$ suggested for porous materials (Bjorkman

Table 1
Material properties based on ANEOS output except as noted.

Material	S_c[a] (J/kg K)	S_i[a] (J/kg K)	P_{cm} (GPa)	P_{cr} (GPa)	P_{im} (GPa)	E_M (J/kg)
Aluminum	2640	2210	106	–	72.6	7.3×10^6
Dunite	3240	3000	156	146	136	1.0×10^7
Granite	2500	2220	51.0	46.7	43.1	4.5×10^6
Ice	3160	2210	5.24	3.751	2.34	9.6×10^5
Iron	1790	1650	391	–	307	1.0×10^7

[a] Pierazzo et al. (1997).

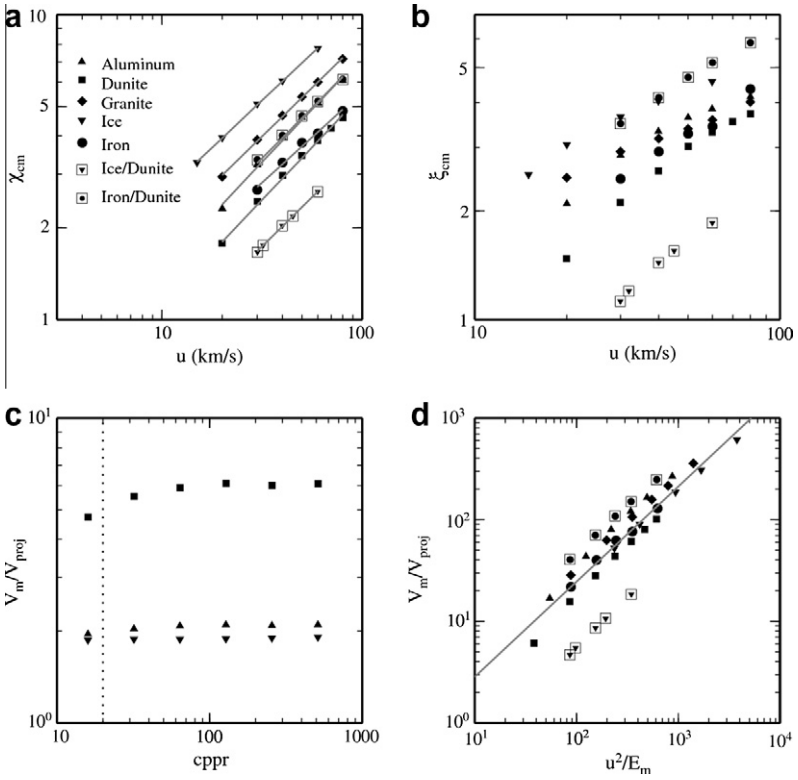

Fig. 1. (a) Radius of the completely melted region for impacts between identical materials (symbols) for aluminum, dunite, granite, ice, and iron. The variation in the radius of the completely melted region as a function of impact velocity is shown for impacts between an iron projectile and dunite target, and ice projectile and dunite target, relevant to cometary and asteroidal impacts on rocky planets. Incipient and 50% melt radii are similar in value and similar in trend with similar slopes (see Table 2). (b) Same as (a) but for the depth of burial of the completely melted region. (c) Variation in melt volume (V_m/V_{proj}) as a function of cppr for a dunite/dunite impact at 20 km/s (square) aluminum/aluminum impact at 20 km/s (triangle), and ice/ice impact at 10 km/s (inverted triangle). Dotted vertical line is the approximate location of 20 cppr, the numerical resolution used by P97. (d) Melt volume as a function of melt number (u^2/E_M). Gray line shows fit to like/like impact data (iron/dunite and ice/dunite data are shown for reference but are not included in the fit).

Table 2
Fitting coefficients for melt region shapes, for use in Eqs. (2) and (3).

Material	Complete melting radius		Complete melting depth of burial		50% Melting radius		50% Melting depth of burial		Incipient melting radius		Incipient depth of burial	
	a_χ	b_χ	a_ξ	b_ξ	a_χ	b_χ	a_ξ	b_ξ	a_χ	b_χ	a_ξ	b_ξ
Aluminum	3.86	0.697	3.15	0.488	–	–	–	–	4.63	0.674	3.44	0.420
Iron	3.23	0.600	2.88	0.558	–	–	–	–	3.56	0.589	3.05	0.540
Dunite	2.90	0.693	2.45	0.728	3.00	0.674	2.52	0.651	3.08	0.677	2.54	0.657
Ice	6.05	0.622	4.04	0.486	6.83	0.614	4.22	0.115	8.73	0.603	4.52	0.425
Granite	4.63	0.641	3.15	0.335	4.83	0.637	3.22	0.321	5.03	0.633	3.27	0.306
Ice/Dunite	2.02	0.651	2.13	0.651	2.07	0.651	1.43	0.712	2.13	0.651	1.46	0.705
Iron/Dunite	3.95	0.666	4.02	0.595	4.23	0.657	4.10	0.580	4.18	0.656	4.17	0.573

and Holsapple, 1987). To search for possible discrepancies between our methods, we performed ice/ice impact simulations using both versions 8.1 and 9.1 of CTH with a geometry, tracer setup, target size, target temperature, and projectile size identical to those used in P97. We find that with a target temperature of 233 K, we obtain r_{cm} comparable to P97, but we are unable to accurately determine the melt volume because for target $T > 215$ K, the target entropy is comparable to the entropy for incipient melting. Thus, the incipient melt region encompasses essentially the entire computational domain. On the basis of these tests, we suggest that the high target temperatures in P97 may have lead to an overestimation of melt volumes in ice/ice impacts.

5. Discussion

In numerical simulations with resolution 50 times higher than prior work, we find shapes and sizes of melt regions, and melt volumes comparable to those calculated at lower resolution by Pierazzo et al. (1997) for all materials, with the exception of ice, where we find melt volumes 10 times lower than reported by P97 owing to a lower target temperature. The results of the P97 study set water ice apart as a material with a manifestly different behavior than metals and rocks. However, our results suggest that scaling of melt volumes and melt region sizes for water ice are similar to those for rocks and metals. We note that impacts in our study are vertical; impact angles >60° significantly decrease melt volumes and distort the shape of the isobaric core (Pierazzo and Melosh, 2000).

We also provide new scalings for melt volumes and information about the size and shape of melted region in vertical ice/dunite and iron/dunite impacts. We find that melt volumes in iron/dunite impacts follow a scaling similar to that for like/like impacts, whereas melt volumes in ice/dunite impacts are substantially lower. A typical dunite/dunite impact commonly assumed for the lunar Late Heavy Bombardment, with an impact velocity ~20 km/s (e.g., Levison et al., 2001; Gomes et al., 2005) will create a completely melted region ~1.8 times the projectile radius. An iron meteorite impact creates a melted region ~2.5 times the impactor radius, but cometary LHB impactors predicted by (Gomes et al., 2005) will create a melt region only ~1.3 times the impactor radius. Thus, the compositional diversity of the LHB may need to be taken into account when converting from crater morphology to impactor size distribution.

Acknowledgments

This work is supported by the NASA Lunar Science Institute through NNA09DB32A. Author Citron acknowledges support from NASA GSRP NNX09AM18H. We thank D. Durda for helpful comments. We also thank E. Pierazzo and O. Barnouin-Jha for helpful reviews.

References

Abramov, O., Kring, D.A., 2005. Impact-induced hydrothermal activity on early Mars. J. Geophys. Res. 110. E12S09. doi:10.1029/2005JE002453.

Abramov, O., Mojzsis, S.J., 2009. Microbial habitability of the Hadean Earth during the Late Heavy Bombardment. Nature 459, 419–422.

Barr, A.C., Canup, R.M., 2010. Origin of the Ganymede-Callisto dichotomy by impacts during the Late Heavy Bombardment. Nat. Geosci. 3, 164–167.

Barr, A.C., Citron, R.I., Canup, R.M., 2010. Origin of a partially differentiated Titan. Icarus 209, 858–862.

Benz, W., Cameron, A.G.W., Melosh, H.J., 1989. The origin of the Moon and the single-impact hypothesis. III. Icarus 81, 113–131.

Bjorkman, M.D., Holsapple, K.A., 1987. Velocity scaling of impact melt. Int. J. Impact Eng. 5, 155–163.

Bottke, W.F., Nesvorny, D., Grimm, R.E., Morbidelli, A., O'Brien, D.P., 2006. Iron meteorites as remnants of planetesimals formed in the terrestrial planet region. Nature 439, 821–824.

Cintala, M.J., Grieve, R.A.F., 1998. Scaling impact-melt and crater dimensions: Implications for the lunar cratering record. Meteorit. Planet. Sci. 33, 889–912.

Croft, S.K. 1982. A first-order estimate of shock heating and vaporization in oceanic impacts. Geological Society of America Special Paper 190, pp. 143–152.

Gault, D.E., Heitowit, E.D. 1963. The partition of energy for hypervelocity impact craters formed in rock. In: Proc. 6th Hypervelocity Impact Symp., vol. 2, pp. 419–456.

Gomes, R., Levison, H.F., Tsiganis, K., Morbidelli, A., 2005. Origin of the cataclysmic Late Heavy Bombardment period of the terrestrial planets. Nature 435, 466–469.

Grieve, R.A.F., Cintala, M.J., 1992. An analysis of differential impact melt-crater scaling and implications for the terrestrial impact record. Meteoritics 27, 526–538.

Kieffer, S.W., Simonds, C.H., 1980. The role of volatiles and lithology in the impact cratering process. Rev. Geophys. Space Phys. 18, 143–181.

Levison, H.F., Dones, L., Chapman, C.R., Stern, S.A., Duncan, M.J., Zahnle, K., 2001. Could the lunar "Late Heavy Bombardment" have been triggered by the formation of Uranus and Neptune? Icarus 151, 286–306.

McGlaun, J.M., Thompson, S.L., Elrick, M.G., 1990. CTH: A 3-dimensional shock-wave physics code. Int. J. Imp. Eng. 10, 351–360.

Melosh, H.J., 1989. Impact Cratering: A Geologic Process. Oxford University Press, New York.

Melosh, H.J., 2007. A hydrocode equation of state for SiO_2. Meteorit. Planet. Sci. 42, 2079–2098.

O'Keefe, J.D, Ahrens, T.J., 1977. Impact-induced energy partitioning, melting, and vaporization on terrestrial planets. In: Proc. Lunar Planet. Sci. Conf. 8, 3357–3374.

Pierazzo, E., Melosh, H.J., 2000. Melt production in oblique impacts. Icarus 145, 252–261.

Pierazzo, E., Vickery, A.M., Melosh, H.J., 1997. A reevaluation of impact melt production. Icarus 127, 408–423.

Pierazzo, E. et al., 2008. Validation of numerical codes for impact and explosion cratering: Impacts on strengthless and metal targets. Meteorit. Planet. Sci. 43, 1917–1938.

Reese, C.C., Solomatov, V.S., 2006. Fluid dynamics of local martian magma oceans. Icarus 184, 102–120.

Renner, J., Evans, B., Hirth, G., 2000. On the rheologically critical melt fraction. Earth Planet. Sci. Lett. 181, 585–594.

Stewart, S., Ahrens, T.J., 2005. Shock properties of H_2O ice. J. Geophys. Res. 110. E03005. doi:10.1029/2004JE002305.

Thompson, S.L., Lauson, H.S., 1972. Improvements in the Chart D Radiation–Hydrodynamic Code III: Revised Analytical Equation of State. SC-RR-710714, Sandia Natl. Lab., Albuquerque, NM.

Tonks, W.B., Melosh, H.J., 1992. Core formation by giant impacts. Icarus 100, 326–346.

Tonks, W.B., Melosh, H.J., 1993. Magma ocean formation due to giant impacts. J. Geophys. Res. 98, 5319–5333.

Tonks, W.B., Pierazzo, E., Melosh, H.J., 1997. Impact-induced differentiation in icy bodies. Icarus, unpublished.

Turtle, E.P., Pierazzo, E., 2001. Thickness of a Europan ice shell from impact crater simulations. Science 294, 1326–1328.